Supplementary material for the manuscript

Formation and composition of secondary organic aerosols from the uptake of glyoxal on natural mineral dust aerosols: a laboratory study

Francesco Battaglia[1], Paola Formenti[1], Chiara Giorio[2], Mathieu Cazaunau[3], Edouard Pangui[3], Antonin Bergé[3], Aline Gratien[1], Thomas Bertin[3], Joel F. de Brito[4], Manolis N. Romanias[4], Vincent Michoud[1], Clarissa Baldo[1,3], Servanne Chevaillier[3], Gael Noyalet[3], Philippe Decorse[5], Bénédicte Picquet-Varrault[3], and Jean-François Doussin[3]

[1] Université Paris Cité and Univ Paris Est Créteil, CNRS, LISA, F-75013 Paris, France

[2] Yusuf Hamied Department of Chemistry, University of Cambridge, Lensfield Road, Cambridge, CB2 1EW, UK

[3] Univ Paris Est Créteil and Université Paris Cité, CNRS, LISA, F-94010 Créteil, France

[4] IMT Nord Europe, Institut Mines-Télécom, Université de Lille, Centre for Energy and Environment, 59000, Lille, France

[5] Université Paris Cité, CNRS, Itodys, F-75013 Paris, France

Table S1. List of target mass fragments for molecules linked to glyoxal reactivity used in the assignment of the SFE/GC-MS mass spectra. The table consists of three columns: the first column shows the masses of the fragments derived from molecules produced by the reactivity of glyoxal and mineral dust which are not present in the NIST library, the second column shows the expected molecular formulas of the fragments, and the third column describes the hypothesized molecular fragmentation pattern.

m/z	Fragment	Assignment
73	$[Si(CH_3)_3]^+$	Fragment from compounds with 1 TMS functionality
117	$[COO=Si(CH_3)_3]^+$	Fragment from compounds with 1 TMS caboxylic functionality
131	$[(CH_3)_2SiO\text{-}C=O\text{-}HC=O]^+$	Glyoxylic acid fragment
147	$[(CH_3)_2Si=OSi(CH_3)_3]^+$	Fragment from compounds with 2 TMS functionalities
205	$[(CH_3)_3SiO\text{-}C=O\text{-}CH_2\text{-}OSi(CH_3)_2]^+$	Glycolic acid fragment
221	$[SiH(CH_3)_2\text{-}C_4H_4O_5\text{-}SiH_2]^+$	Glyoxal dimer fragment – 3*CH_3 + 3H
235	$[Si(CH_3)_3\text{-}C_4H_4O_5\text{-}SiH_2]^+$	Glyoxal dimer fragment – 2*CH_3 + 2H
263	$[Si(CH_3)_3\text{-}C_4H_4O_5\text{-}Si(CH_3)_2]^+$	Glyoxal dimer fragment from Gly hydrated ($C_2H_4O_3$) + Gly dihydrated ($C_2H_6O_4$) = $C_4H_6O_5$
281	$[Si(CH_3)_3\text{-}OSi(CH_3)_2\text{-}OSi(CH_3)_2\text{-}OSi(CH_3)H]^+$	Fragment from siloxane like compounds -> peak generated by GC column residues

Table S2. List of filter samples collected for SFE and Orbitrap analyses and the experimental conditions associated.

Conditions	ID	Date	RH	Light	Ox	Orbitrap	SFE
D	D_1	31/01/2022	Dry	dark	---	**X**	**X**
				light	---	**X**	**X**
D	D_2	03/02/2022	75%	dark	---	**X**	**X**
				light	---	**X**	**X**
D + GL	D_3	04/02/2022	Dry	dark	---	**X**	**X**
				light	---	**X**	**X**
	D_4	08/02/2023	32%	dark	---		**X**
	D_5	09/02/2023	31%	light	---	**X**	**X**
	D_6	10/02/2023	35%	dark	---	---	**X**
	D_7	13/02/2023	34%	light	---	---	**X**
	D_8	30/04/2021	76%	light	---	---	---
	D_9	03/05/2021	79%	light	---	---	---
	D_{10}	04/05/2021	81%	light	---	**X**	---
	D_{11}	05/05/2021	78%	dark	---	**X**	---
	D_{12}	06/05/2021	82%	dark	---	**X**	---
	D_{13}	08/02/2022	81%	dark	O_3	**X**	**X**
				light		**X**	**X**
	D_{14}	09/02/2022	78%	dark	O_3	---	---
				light		**X**	**X**
	D_{15}	10/02/2022	75%	dark	---	---	---
				light	---	**X**	**X**
	D_{16}	14/02/2023	83%	dark	---	**X**	**X**
	D_{17}	15/02/2023	75%	light	---	---	**X**

Figure S1. Result of XPS analysis of a filter sample collected during one ageing experiment of Gobi dust with glyoxal, at 80% RH (experiment D15 in Table S1). Left: XPS spectrum and derived atomic percentages. Right: zoomed view of the most prominent peaks, adn their attribution. From top to bottom, and left to right: Si2p attributed to quartz in mineral dust, C1s from the C-F bond of the Teflon filter (297 eV) and from carbon in the aerosols, O1, and F1s from the C-F bond of the Teflon filter.

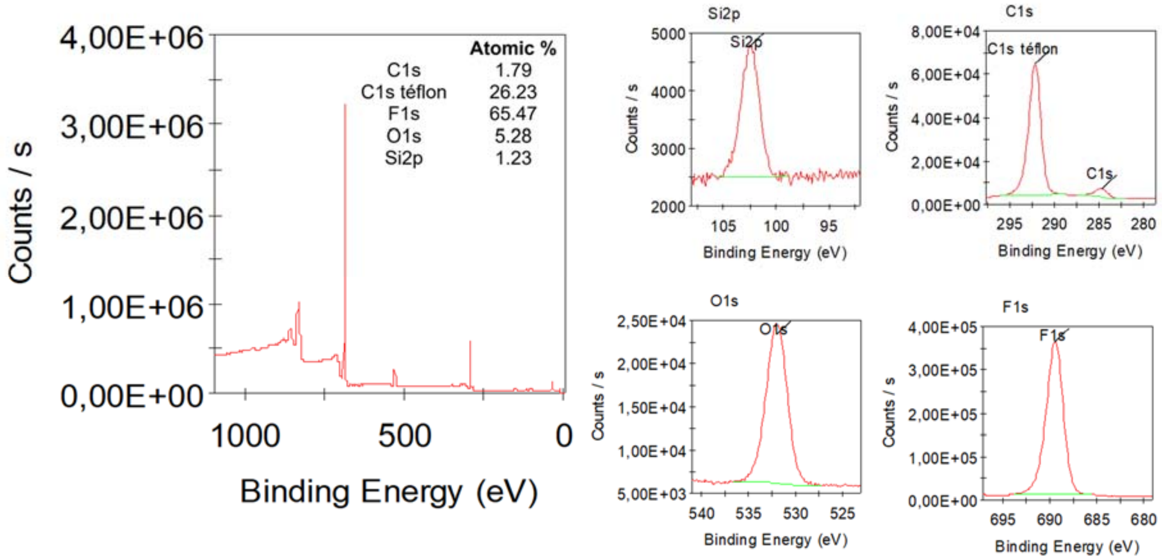

Figure S2. Comparison of the time series of the logarithm of POM concentration (normalised to the initial value POM0), upper panel, and the total volume concentration (normalised to the initial value Vol0), lower panel. Time is calculated since the end of the dust injection. The slope of the linear decrease during the evaporation phase (straight solid lines) is indicated.

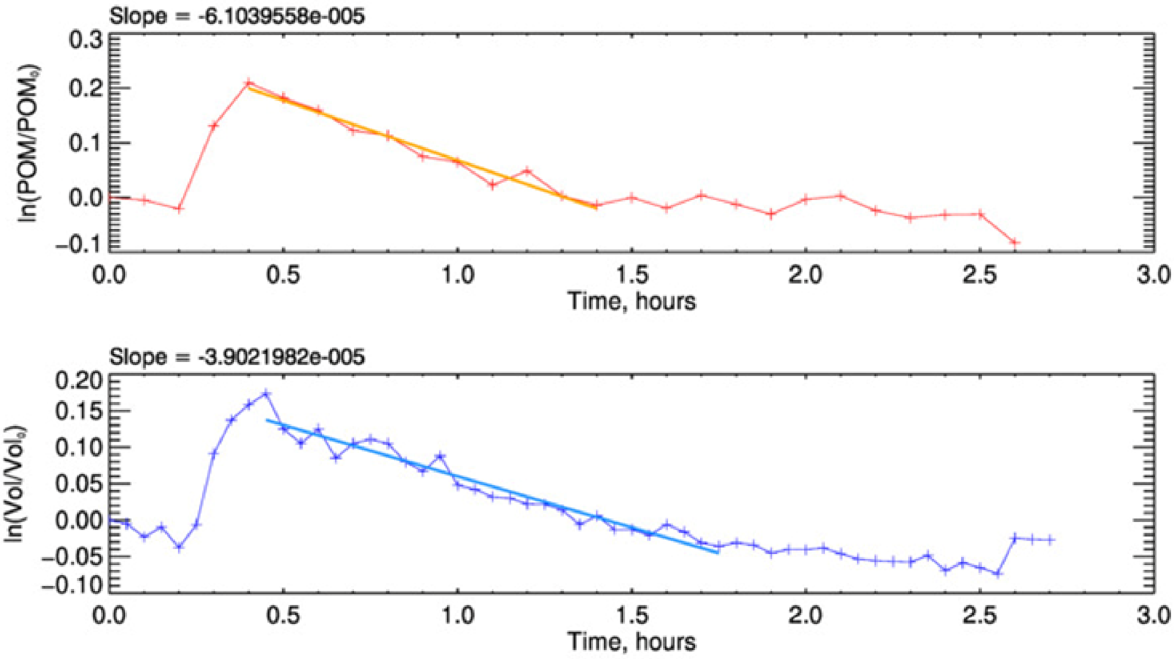

.

Figure S3. NO and NO_2 concentrations measured during the injection of water vapour in experiment D15. The shaded area corresponds to the injection of dust into the chamber, during which the instruments were disconnected. The yellow-highlighted portions indicate the interval where irradiation takes place. Wang et al. (2011) have shown that the chamber walls may act as a reservoir of a NO and HONO, that can be rapidly desorbed during the injection of water vapour. Upon irradiation, the desorbed HONO may act as a source of OH radicals, which in turn facilitate the rapid conversion of NO to NO_2.

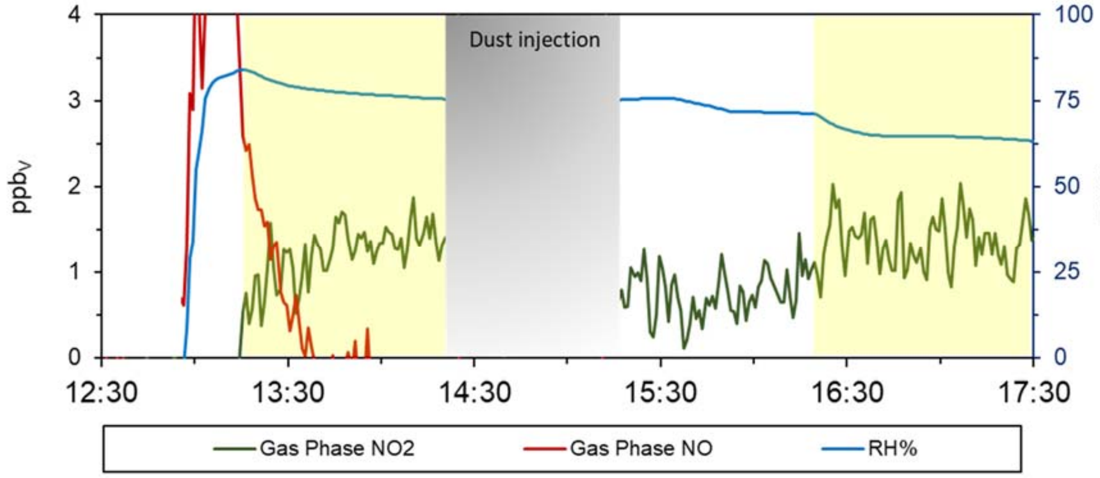

Figure S4. Time series of O/C ratio measured by the ACSM (black line) during ageing with glyoxal in dry conditions (top, experiment D_3) and at 30% RH (bottom, experiment D_7). The black arrows show the duration of filter sampling and the corresponding O/C values obtained by XPS analysis. The yellow-highlighted portion of the graph indicates the interval where irradiation takes place, while the green vertical dashed lines indicate the moment of glyoxal injection in the chamber.

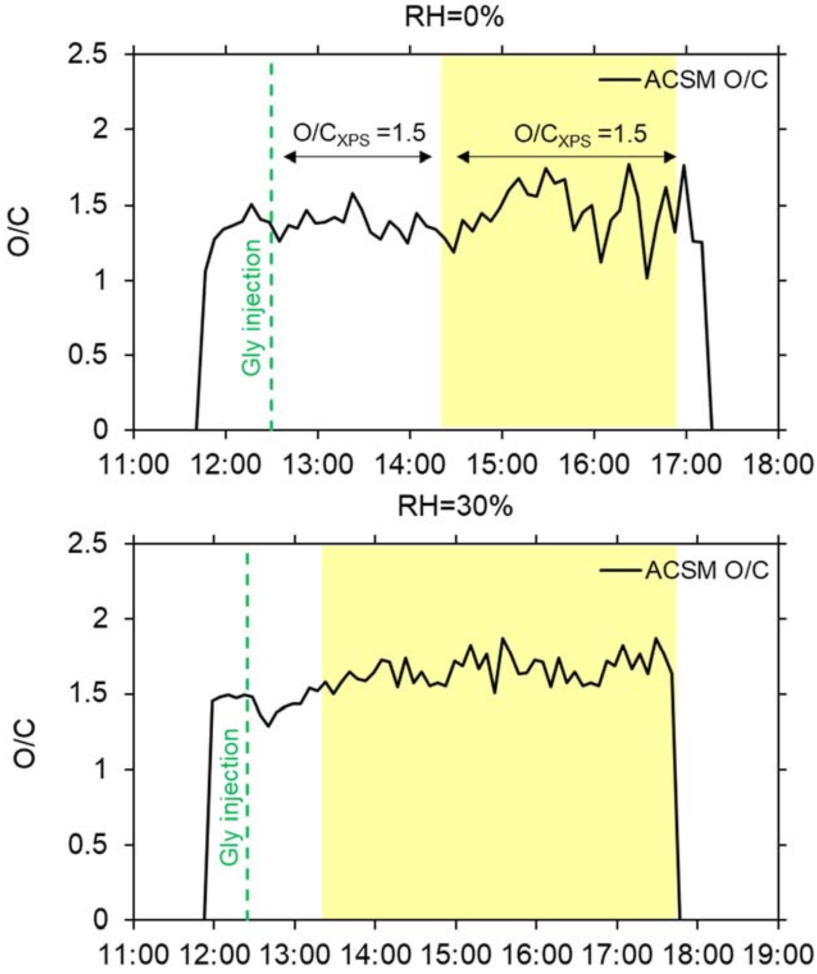

Text S1. New particle formation from water irradiation

Water vapor used for ageing experiments is produced by heating water from an ultrapure water generation system (Milli-Q IQ 7000, Merk™), which contains a certain level of organic carbon contamination, typically in the range of 2-3 µg L^{-1} (measured from the ultrapure water generation system). This gaseous organic carbon introduced with the water vapor might oxidize and form new particles, adding to the background organic aerosol concentration and affecting the measurements of aerosol growth and transformation. The consequence of this contamination is the potential formation of additional particles that could interfere with the experimental results. This could lead to an overestimation of particle formation from the intended experimental reactions, complicating the interpretation of the number and mass concentration and the molecular composition data. Therefore, it is crucial to characterize this potential contamination to ensure the accuracy and reliability of the experimental findings.

To assess the potential oxidation and formation of new organic aerosol particles, the system was irradiated immediately after water vapor injection. This process consistently led to the generation of new particles, detected solely by the CPC, as the SMPS, with a lower detection limit of 19.5 nm, was unable to register them. Consequently, these particles stem from the oxidation of organics present in the water vapor and are notably smaller, with diameters typically below 20 nm. Before introducing the dust, sufficient time was allowed for the removal of those particles from the simulation chamber (Figure S1.1).

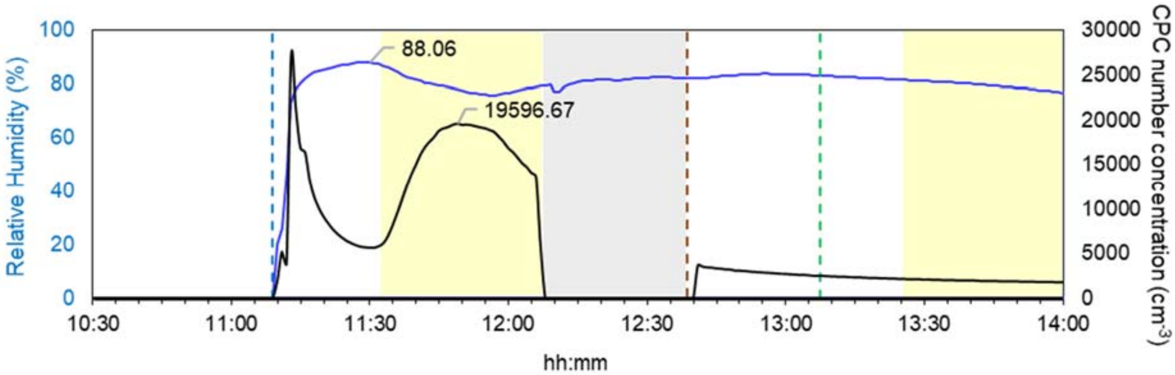

Figure S1.1. Total particle number concentration (black line) measured by the CPC instrument following the injection water vapour, indicated by a vertical blue bar, for one experiment conducted at 80% RH (blue line). The irradiation is indicated by the vertical yellow bars. The vertical orange bar indicates the time of injection of mineral dust particles. The vertical green bar indicates the time of injection of glyoxal. The grey area indicates the time interval where the instruments were disconnected for dust injection. The TOC of the ultrapure water injected for this experiment was 2.2 µg L^{-1}.

However, to assess the impact of this contamination and explore the hypothesis of its origin from the total organic carbon (TOC) content of the injected water, we calculated its mass contribution with two approaches and compared the results:

The maximum total organic carbon concentration (TOC_{max}) that can be found in the chamber as a result of the water vapor injection can be estimated as

$$TOC_{max} = \left(\frac{w_{H_2O}}{w_{air}}\right) \times \left(\frac{\rho_{air}}{\rho_{H_2O}}\right) \times TOC_{H_2O} \qquad \text{(S1.1)}$$

where the ratio w_{H2O}/w_{air} is the percent mass fraction of water vapour introduced in CESAM at the maximum inner relative humidity and corresponding temperature (in this example 88%RH and 17°C, respectively), ρ_{air} and ρ_{H2O} are the corresponding air and the water densities (1.225 kg m^{-3} and 1 g cm^{-3}, respectively; (Jung and Schindler, 2019)), and TOC_{H2O} is the total organic carbon measured by the ultrapure water generation system (average of 2.2 µg L^{-1}). The calculation of the w_{H2O}/w_{air} ratio is done with the Humidity calculator application (https://humiditycalculator.vaisala.com/).

Figure S1.1 shows that the injection of water vapour is followed by a rapid and significant increase in the total number of particles, reaching a maximum value of about 27000 cm^{-3}. Upon reaching this maximum value, concentration decreases quickly due to the combined effect of dilution but mostly coagulation, down to a plateau value of approximately 5000 cm^{-3}. At this moment, lights are turned on and the particle concentration increases again up to approximately 20000 cm^{-3}, indicating that new particle formation due to photochemistry of the residual organic content in the gas phase is occurring. No particles are observed by the SMPS (lower sizing limit of 19.5 nm). At this moment, the maximum mass particle concentration observed in the chamber can be calculated assuming a monodispersed particle distribution centered at an average diameter d_p of 10 nm as

$$N_{new} = \frac{4}{3}\pi \, {d_p}^3 \, \rho_p \ N_{CPC} \qquad \text{(S1.2)}$$

Where N_{CPC} is the total number concentration measured by the CPC and ρ_p is the particle density, assumed equal to 1.2 (Kostenidou et al., 2007).

Finally, Figure S1.1 shows that the particle concentration starts decreasing after approximately 10 minutes, despite irradiation is ongoing, suggesting that all the organic gas phase had undergone oxidation, and that coagulation and dilution are overtaking production. At this moment, approximately 5000 particles cm^{-3} are observed by the SMPS below 100 nm diameter, and a total mass concentration of 160 ng m^{-3} (not shown). The mixing volume is further diluted to perform the dust injection (grey bar in Figure S1.1.). By this procedure, the mass concentration finally measured by the SMPS in the size range smaller than 100 nm is 70 ng m^{-3}. For comparison, the dust mass concentration injected during this experiment is 102 µg m^{-3} (Table 1, assuming a density of 2.65 g cm^{-3}), for a minimum diameter of 150 nm.

Figure S1.2 summarizes the comparison of the calculations of TOC_{max} and N_{new}.

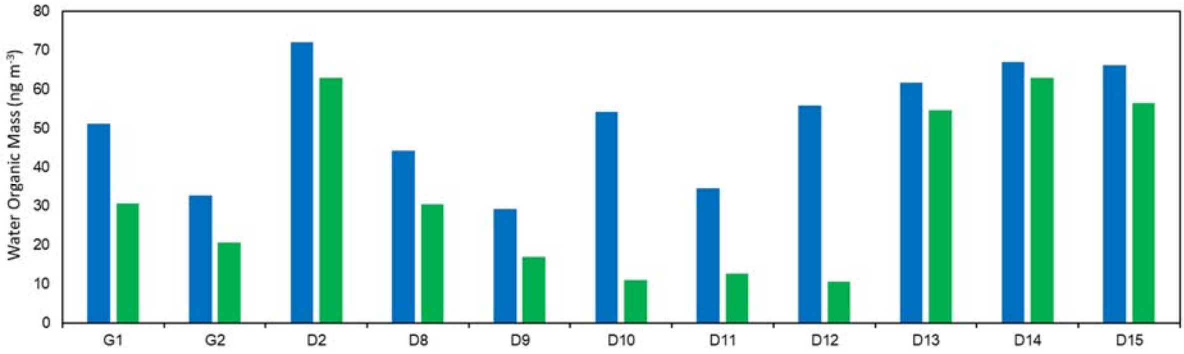

Figure S1.2. Results of Mass Concentration Calculations for 11 Experiments Post Water Injection and Irradiation including experiments with glyoxal only (experiment type GL), dust only and dust aged with glyoxal (D). The blue bars represent the organic masses calculated based on the relative humidity (RH) in the chamber from TOC_{max} calculated by Eq. 3.1, while the green bars indicate the masses calculated from the measured particle concentration measured by the CPC as SOA_{NPF} from Eq. 3.2.

The good agreement between the organic mass calculations supports the hypothesis that the aerosol originates from the oxidation of the TOC in the ultrapure water. The calculated mass concentration of organic particles is approximately one thousand time lower than the mass concentration of dust injected into the chamber, and the size distributions are not overlapping.

Text S2. Correction for the dilution, wall loss and particle loss

S2.1 Dilution correction

The dilution of the gas-phase compounds and aerosol particles in the chamber during the experiments is due to the injection of particle-free nitrogen flow, which is needed to equalise the flow extracted by the instruments and keep the pressure constant in the chamber. The differential decrease in concentration due to dilution ($\Delta C_{dilution_{t_n}}$) in a generic time interval from t_{n-1} to t_n is calculated according to the procedure described in Denjean et al. (2015) as:

$$\Delta C_{dilution_{t_n}} = C_{t_{n-1}} \cdot \left(-\frac{Q_{t_{n-1}}}{V_{chamber}}\right) \cdot e^{-\left(\frac{Q_{t_{n-1}}}{V_{chamber}}\right)\cdot(t_n - t_{n-1})} \cdot (t_n - t_{n-1}) \qquad \text{(S2.1)}$$

where $C_{t_{n-1}}$ is the concentration measured at time t_{n-1}, $\frac{Q}{V_{chamber}}$ is the dilution rate constant in the chamber (s^{-1}), with Q being the compensation air flow ($L\ s^{-1}$) and $V_{chamber}$ the inner volume of CESAM (4200 L).

S2.2 Particle losses

Beside dilution, aerosol particles undergo size-dependent losses due to interactions with the chamber walls (wall losses) and the connecting tubes to the instruments (particle losses). The corrected particle concentration within the chamber can be estimated as

$$C(D)_{corrected_{t_n}} = \left(C(D)_{measured_{t_n}} - C(D)_{measured_{t_{n-1}}}\right) - \Delta C(D)_{dilution\&wall\ loss_{t_n}} \qquad \text{(S2.2)}$$

S2.2.1 Wall losses

The size-dependent particle wall losses are caused by the collisions of the particles with the chamber walls. The differential increase in concentration due to wall loss ($\Delta C_{wall\ loss_{t_n}}$) in a generic time interval t_{n-1} to t_n can be calculated as:

$$\Delta C(D)_{wall\ loss_{t_n}} = W_{t_{n-1}}(D) \cdot \left(-wlr(D)\right) \cdot e^{-wlr(D)\cdot(t_n - t_{n-1})} \cdot (t_n - t_{n-1}) \qquad \text{(S2.3)}$$

where *wlr*(*D*) indicates the size-dependent wall loss rate constant (s^{-1}). Figure S2.1 shows *wlr*(*D*) calculated for mineral dust particles (mass density 2.65 g m^{-3}) adapting the model of Lai and Nazaroff (2000) to the CESAM chamber, as discussed in Lamkaddam (2017).

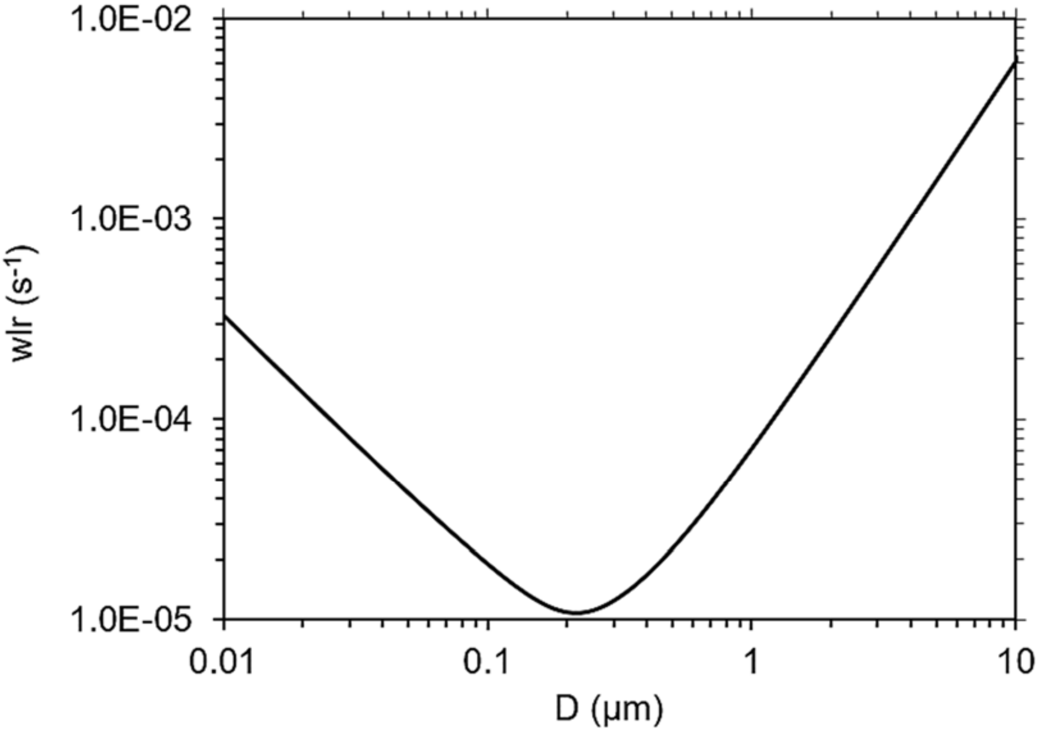

Figure S0.3. *Size-dependent wall loss calculated of mineral dust particles (density of 2.65 g cm^{-3}) in CESAM.*

For instruments that provide size-integrated concentrations (e.g., ACSM), the wall loss correction was calculated by as the ratio between the calculated size-integrated concentration estimated on their working range from SMPS/Sky-GRIMM OPC measurements, and the measured concentration as

$$\%(wall\ loss)_{t_n} = \frac{C_{corrected\ wall\ loss_{t_n}}}{C_{measured_{t_n}}} \tag{S2.4}$$

S2.2.2 Aspiration and transmission losses

The size-dependent losses ($L(D_i)$) of aerosol particles between the chamber and the instruments are due to losses in the connection tubes when the particles are aspirated from the chamber (sampling losses) and while the particles within the tubes (transmission losses). These can be corrected using the Particle Loss Calculator (PLC; Von der Weiden et al., 2009) using as input the geometry of the sampling line, the sampling flow rate, the particle shape factor, and the particle density. The particle loss functions for the sampling lines of the SMPS, Sky-GRIMM, CPC and ACSM are illustrated in Figure S2.2.

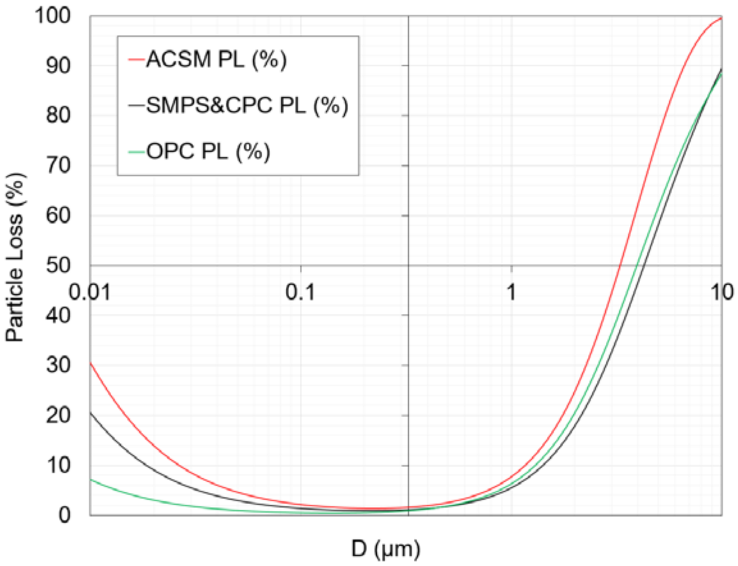

Figure S0.4. Size dependent Particle Loss (PL; %) calculated for mineral dust aerosols for the sampling lines connecting the simulation chamber atmosphere to ACSM (red line), OPC (green line), SMPS (black line), and CPC (black like). For mineral dust, the density used for calculations is 2.65 g cm^{-3}.

Figure S2.2 shows the on the size range of interest of this work (0.1 – 1 μm), the particle losses are minor (within 6%) and most important almost equal from one instrument to the other, which makes the various measurements comparable. For these reasons, particle loss corrections were not applied to the measured particle concentrations.

Text S3. Control experiments of glyoxal with ammonium sulphate particles

Five control experiments using ammonium sulphate as seeds were conducted at 30 and 80% RH to validate the experimental protocol. Table S3.1 summarizes the control experiments and the associated conditions.

Table S3.1. Control experiments using ammonium sulphate seed particles at 30% and 80% RH to validate the experimental protocols of glyoxal-dust interaction. Conditions include date, experiment ID, relative humidity (RH), light conditions, initial ozone ($[O_3]_i$) and glyoxal ($[Gly]_i$) concentrations in parts per billion volume (ppbv), temperature (Temp (K)), and initial volume concentration of seed particles ($Vseed_i$) in cubic micrometers per cubic centimeter ($\mu m^3\ cm^{-3}$). Initial concentrations ($[O_3]_i$, $[Gly]_i$ and $Vseed_i$) are referred to the maximum concentrations recorded after the injection.

Conditions	**Date**	**ID**	**RH**	**Light**	**$[O_3]_i$ ppb_v**	**TempK**	**$[Gly]_i$ ppb_v**	**$Vseed_i$ μm^3 cm^{-3}**
AS+GL	21/02/2023	AS_1	38%	dark	---	298	527	50.13
AS+GL	23/02/2023a	AS_2	35%	dark	---	298	516	48.34
AS+GL	23/02/2023b	AS_3	32%	light	---	298	445	64.81
AS+GL	07/02/2023	AS_4	81%	light	---	301	2000	304.09
AS+GL	08/02/2023	AS_5	83%	light	---	300	1000	161.17

Ammonium sulphate particles were generated by vaporizing a solution of 0.1 M high-purity ammonium sulphate (Sigma-Aldrich, 99.99%) using a constant-output atomizer (model 3076, TSI Inc., Shoreview, MN, USA) with at a nitrogen flow of 2 L min^{-1}. Prior entering the chamber, the solution was dried using a diffusion dryer (model 3062, TSI Inc., Shoreview, MN, USA) and size-selected using the AAC (D_m = 400 nm, k = 1770 kg m^{-3}, f = 3) with a sheath flow of 8 L min^{-1}. Unlike the dust injection protocol, it was not necessary to modify the internal chamber pressure to achieve a sufficient inflow of ammonium sulphate particles.

The timeline of the experiments is shown in Figure S3.1, presenting a time series of normalized intensities for various organic fragments detected by the ACSM, specifically m/z 58, 68, 105, 44, and total organic, normalized against the sulphate signal. These specific signals are chosen because they serve as key markers for different aspects of glyoxal chemistry: m/z 58 is a marker for glyoxal itself, m/z 105 indicates glyoxal oligomers, m/z 68 represents imidazole-like CHNO structures formed through the glyoxal-ammonium sulphate reaction, and m/z 44 is commonly associated with secondary organic aerosol formation.

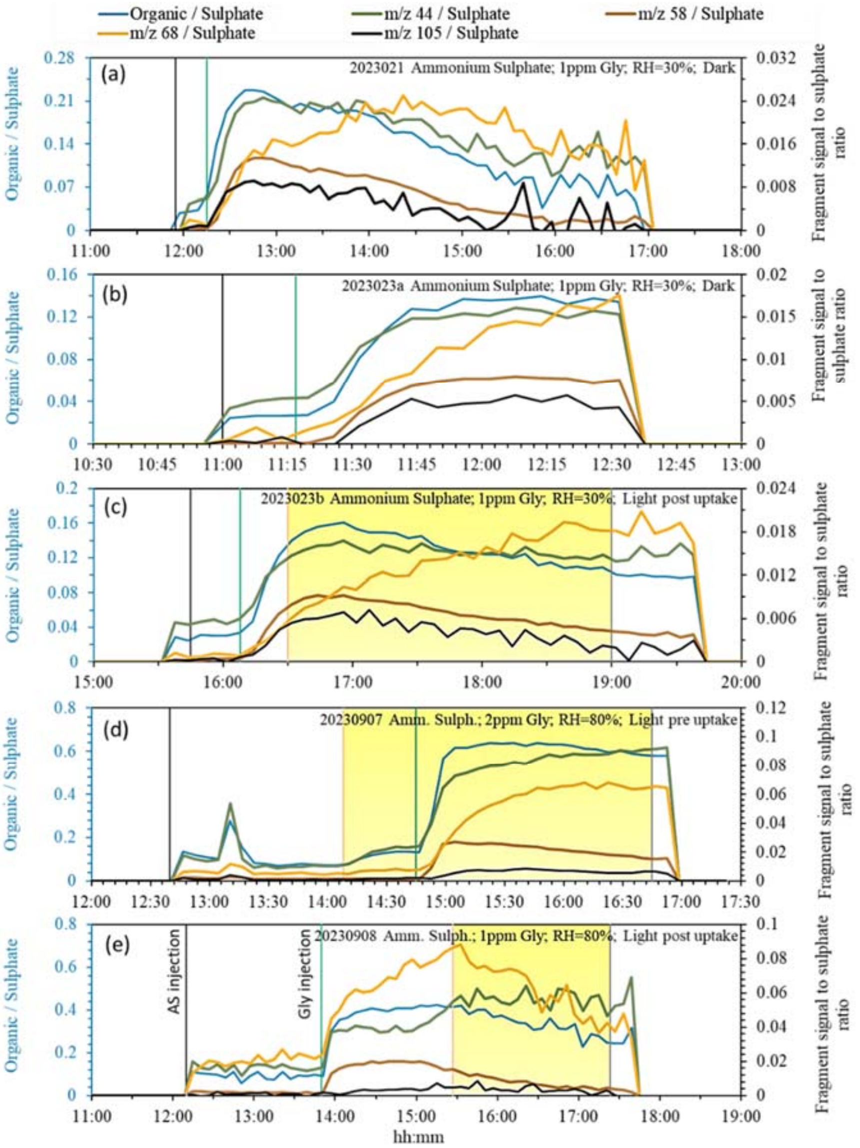

Figure S3.5. The time series of total organic, m/z 58, 105, and 68 fragment ions normalized by the sulphate ion signal for glyoxal uptake experiments. They mimic the graphical representation of the dilution experiments conducted in the study of Galloway et al., 2009. In our study, dilution begins almost instantaneously after glyoxal injection, as it is quantitatively lost on the walls of the chamber within a few minutes. (a) glyoxal uptake on AS at 30% RH in dark conditions, (b) glyoxal uptake on AS at 30% RH in dark conditions, (c) glyoxal uptake on AS at 30% RH under irradiated conditions after, (d) glyoxal uptake on AS at 80% RH under irradiated conditions, (e) glyoxal uptake on AS at 80% RH under irradiated conditions.

This graphical representation mirrors the dilution experiments described by Galloway et al. (2009) to track the dynamics and transformations of glyoxal and its reaction products in the aerosol phase. Galloway et al. (2009) examined the behaviour of glyoxal (GL) uptake and secondary organic aerosol (SOA) formation by monitoring the time traces of total organics and specific fragment ions (m/z 58, 105, and 68) normalized by the sulphate ion signal. Their experimental protocol consisted in injecting glyoxal continuous until reaching the equilibrium with the walls, when the seed aerosols are injected. As a consequence, the formation of SOA occurs on a longer time scale, and reaches a maximum after approximately 10 hours. Figure S3.2 presents the time traces of glyoxal concentration, total organics, and specific fragment ions from two experiments in dark and irradiated conditions. At the point of glyoxal dilution, indicated by a black vertical line, the normalized signals for total organics and GL marker ions (m/z 58 and 105) decreased by 30% and 17%, respectively, suggesting that the uptake of glyoxal is reversible.

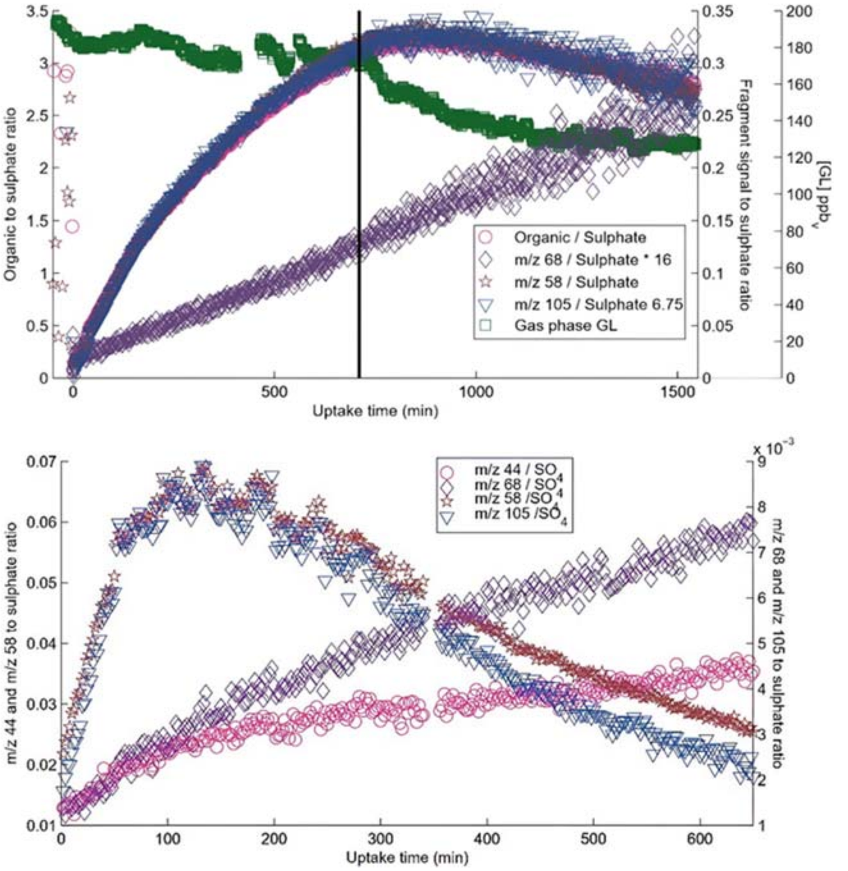

Figure S3.6. Time traces of glyoxal concentration, total organics, and specific fragment ions from Galloway et al. (2009). (Top) Figure 6 shows the time traces of glyoxal concentration, total organics, and specific fragment ions (m/z 58, 105, and 68) normalized by the sulphate ion signal in a dark experiment. (Bottom) Figure 7 displays the time traces of fragment ions (m/z 44, 58, 105, and 68) normalized by the sulphate ion signal in an experiment under irradiated conditions.

Figure S3.2 shows that the behaviour of the m/z 68 marker, associated with imidazole, is different as its uptake is irreversible. This is also true for m/z 44 under irradiation conditions, suggesting that the organic fraction of the aerosol continues to be oxidised with time. This is observed in our experiments too, in particular at 80%, when irradiation promote the 44 m/z signal with respect to the dark conditions. This effect is observed at 30%, but less pronounced. This suggests that irradiation od the AS/glyoxal system increases upon irradiation.

Similar to what observed in Galloway et al. (2009), in our experiments, after the peak of glyoxal uptake, the normalized organic concentration and tracer signals of glyoxal and its oligomers (58 and 105 m/z) decreases over time, suggesting that the uptake is reversible. The behaviour of imidazole is different from that observed by Galloway, as in our experiment this compound shows a reversible uptake, albeit at a slower rate than fragments 58 and 105. We attribute this difference to the fact that, in our study, we performed a single injection of glyoxal, which is then rapidly lost from exchanges with the walls, particularly at 80%RH.

In addition to m/z= 44, 58, 68 and 105, Galloway et al. (2009) observed significant fragments at 29, 77, 88, 117, 135, 145, and 175 m/z. These fragments are associated with precursor structures originating from glyoxal, along with its hydration and oligomerization products, which aligns with the findings from Liggio et al. (2005a).

Figure S3.3 illustrates the ACSM organic fraction mass spectra recorded at maximum glyoxal uptake on ammonium sulphate experiments.

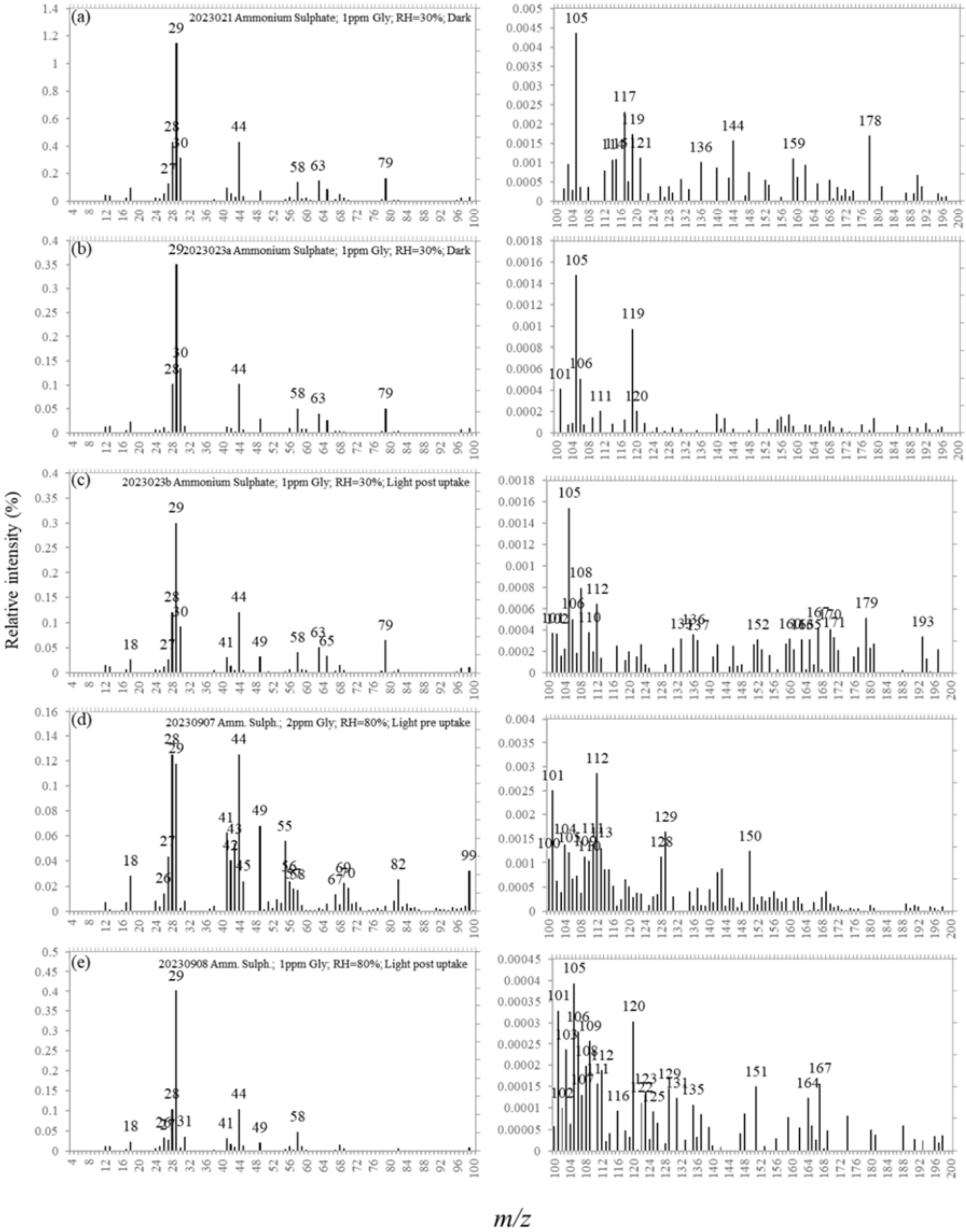

Figure S3.7. ACSM organic fraction mass spectra recorded at maximum glyoxal uptake on ammonium sulphate experiments: (a) glyoxal uptake on AS at 30% RH in dark conditions, (b) glyoxal uptake on AS at 30% RH in dark conditions, (c) glyoxal uptake on AS at 30% RH under irradiated conditions after, (d) glyoxal uptake on AS at 80% RH under irradiated conditions, (e) glyoxal uptake on AS at 80% RH under irradiated conditions.

Beside the major fragments 29, 58, 30 and 44 m/z, the 79 *m/z* fragment is observed during 3 out of 5 experiments, and attributed to organosulphates by Galloway et al. (2009). No significant differences are observed at different relative humidity nor according to irradiation.

S3.1. Conclusions

Five control experiments using size-selected ammonium sulfate particles at relative humidity between 30% and 80% were conducted to validate the experimental protocol for glyoxal-particle interactions. The results showed that the glyoxal uptake dynamics on AS align with previous studies, providing strong support for the reliability of our experimental setup.

We observed a rapid uptake process that reached its maximum within less than 10 minutes. This is notably faster than what was reported in the studies we used for comparison, such as those by Galloway et al. (2009) and Liggio et al. (2005a). The difference in interaction time stems from the shorter lifetime of glyoxal in our experimental chamber, as it is quickly lost to chamber walls.

Despite this, the overall organic aerosol composition we observed were comparable to what has been previously reported.

Our findings parallel those of Galloway et al. (2009), especially in terms of the formation of imidazole-like structures (m/z 68) and organosulphates (m/z 79). Additionally, as in the reference study, we observed that the imidazole-like structures (m/z 68) exhibited reversible uptake compared to glyoxal and its oligomers (m/z 58 and 105). The overall composition of organics recorded by the ACSM, especially the presence of key fragments like m/z 44 under irradiated conditions at higher humidity, confirmed the continuous oxidation processes occurring in line with what has been reported in similar studies.

Text S4. Content and composition of the organic fraction in the native Gobi dust aerosols

Control experiments on monodisperse submicron dust aerosol particles without chemical interaction were conducted in dry conditions, at 50% and 80 RH% to evaluate the quantity and the composition of native organic fraction.

S4.1. Organic content

The average ratio of the organic mass with respect to the total dust mass (F_{org}) is 5.1 ± 0.4 for RH < 12%, and 5.4 ± 0.8 for RH at 80%. These percentage values align well with values reported in the literature for soils and windblown dust samples. It should be noted that references mostly concern ambient measurements and the organic content measured there also be affected by atmospheric ageing. O'Sullivan et al. (2014) reported a mass fraction of organic carbon (OC) ranging from 2.5% to 2.9% in agricultural soils. For soil samples sieved to less than 63 µm from Asia and Europe the percent OC content range from 0.7% to 12% (Conen et al. 2011). For soil samples from the US in the submicron fraction, Tobo et al. (2014) reported a higher concentrations of organic compounds (37%). For airborne aerosols, Lepple and Brine (1976) measured an average mass fraction of the sum of C, H, and O atoms of 4.1% in samples from North Africa. Gonçalves et al. (2014) reported that the percent fraction of OC represented less than 2% of the total PM_{10} mass for dust events measured in Cape Verde Islands, downwind the northern and western African source areas. In the Azorean Island, Alves et al. (2007) reported a percent mass concentration of total carbon (sum of organic elemental carbon) with respect to the PM_{10} mass is in the range 1-3% during dust episodes. The OC mass fraction is higher in aerosols produced by agricultural soils, as reported by Pereira et al. (2022) who estimated it in the range 5-17% of the total PM_{10} mass in Mexico and Chili. Simoneit (1980) found that between 0.5% and 2.2% of the mass of aeolian dust is represented by humic substances, associated with primary biogenic residues such as n-alkanes, n-fatty acids, and n-alcohols. The results of a one-year source apportionment conducted by Srivastava et al. (2018) indicate that mineral dust contributes to 13% of the annual average OC, composed of 17-26% humid-like substances, some of which from primary emissions. Aymoz (2004) detected the presence of carboxylic acids on Saharan dust, including oxalate, formate, succinate, and malonate, while Griffin (2007) reviews the presence of organic constituents of microbiological origin in dust from various regions.

S4.2. Organic composition

Figure S4.1 compares the mass spectra measured by the ACSM in dry and humid conditions (50% and 80%), with and without irradiation.

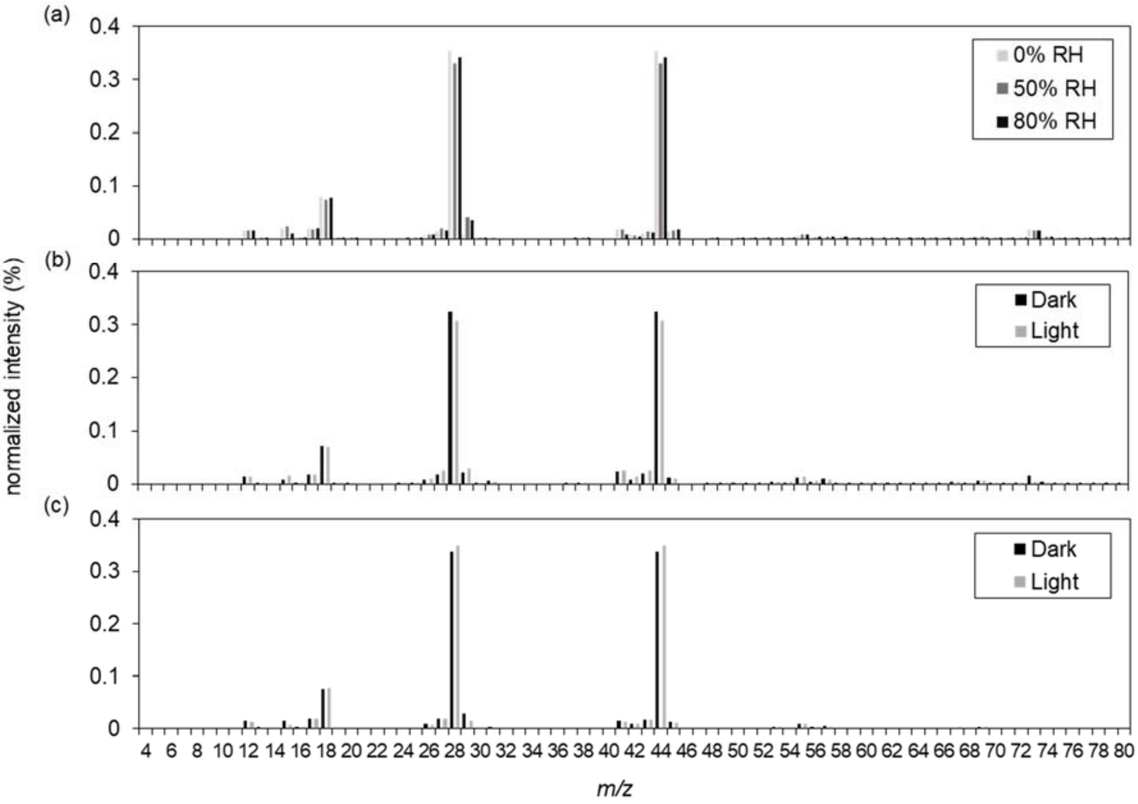

Figure S4.1. Organic mass spectra measured by the ACSM depicting the composition of the organic fraction of Gobi dust under different experimental conditions. The spectra are shown for (a) Gobi dust measured outside the chamber under three different relative humidity (RH) conditions, (b) Gobi dust within the chamber under dry conditions, comparing dark and irradiated states, and (c) Gobi dust within the chamber at 80% RH, also comparing dark (black bars) and irradiated states (light gray bars). The x-axis represents the mass-to-charge ratio (m/z) and the y-axis shows the normalized intensity of detected organic fragments.

The most intense peaks consistently appear at m/z = 18, 28, and 44, across all conditions. The peak at m/z = 18 corresponds to water (H_2O), a known fragment in mass spectrometry that can increase under higher RH conditions. Peaks at m/z = 28 and m/z = 44 represent oxygenated organic compounds. Overall the organic composition of Gobi dust appears to be remarkably consistent in terms of oxidation state. Whether the dust is subjected to different levels of relative humidity or to light exposure, no noticeable changes in the organic fraction is observed in dry conditions. In addition, the stability of the m/z 18 fragment across different relative humidity conditions suggests that Gobi dust particles maintain limited but measurable hygroscopicity. The comparison also shows that the chamber conditions do not affect the organic composition of the dust, as the measurements compare very well with those performed with the simplified setup.

S4.2. ESI Orbitrap

Table S4.1 presents the quantity of particulate organic matter (POM) estimated by integrating the mass concentration measured by the ACMS over the time period of the filter collection, alongside the number of signals detected through ESI Orbitrap analysis.

Table S4.1. Particulate organic matter (POM) collected on filters and the number of ESI Orbitrap peaks detected under varying conditions of Gobi dust, including dry and humid (80% RH) environments, with exposure to light or dark.

Conditions	POM (µg)	Number of ESI Orbitrap peaks detected
Gobi dust, dry, dark	0.4	270
Gobi dust, dry, light	0.3	145
Gobi dust, 80% RH, dark	0.9	102
Gobi dust, 80% RH, light	0.8	86

The POM concentration is low regardless of the collected on the filters varies across different conditions, with the highest POM observed under dark, humid conditions (0.9 µg) and the lowest under dry, light conditions (0.3 µg). In particular, POM decreases in light conditions because the filters were collected later on the same day, following the dark condition experiments, which resulted in the chamber containing a lower mass of aerosol. Additionally, the POM values are at the lower limit of the working range for ESI-MS analysis, which could affect the sensitivity and reliability of peak detection.

The Orbitrap mass spectra collected in dry conditions and at 80%RH, with and without irradiation are shown in Figure S4.2.

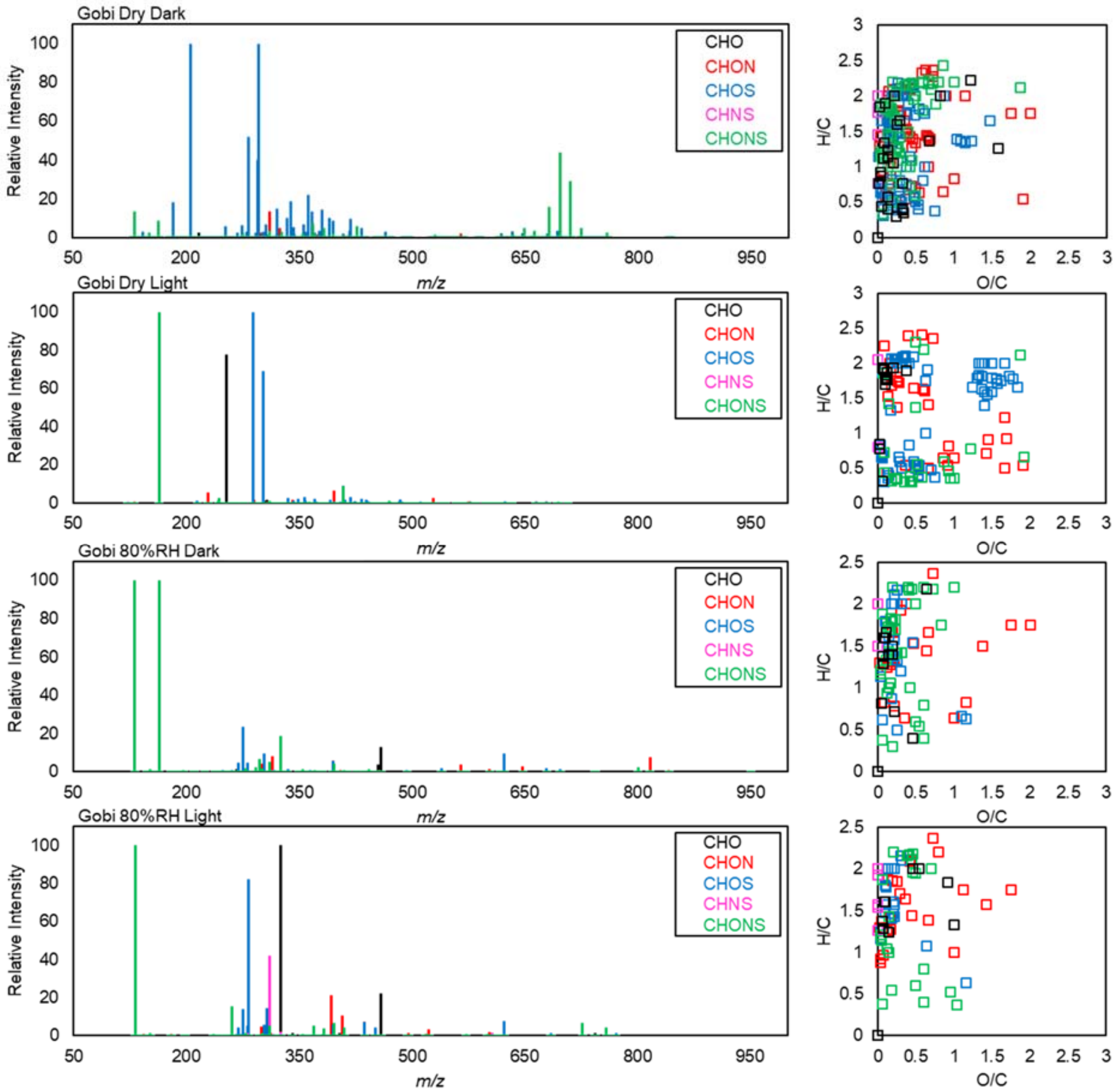

Figure S4.2. Orbitrap mass spectra and van Krevelen diagrams illustrating the organic content of aerosols collected under four distinct conditions: dry conditions without and with light exposure and at 80% RH without and with light exposure. The left panels display the mass spectra; the right panels are the corresponding van Krevelen diagrams. In these spectra, different colours correspond to specific classes of compounds: black for CHO (carbon, hydrogen, oxygen), red for CHON (carbon, hydrogen, oxygen, nitrogen), blue for CHOS (carbon, hydrogen, oxygen, sulphur), purple for CHNS (carbon, hydrogen, nitrogen, sulphur), and green for CHONS (carbon, hydrogen, oxygen, nitrogen, sulphur). These colour code is consistent across both the mass spectra and the van Krevelen diagrams.

The molecular composition of the native dust from the ESI Orbitrap measurements show a low number of peaks (Table S4.1) due to the low organic load on the filters (Table S4.1) and a possible signal suppression due to matrix effects. The mass spectra under dry conditions reveal a complex mixture of compounds, particularly with prominent peaks in the lower m/z range (<500 m/z), with a predominance of CHON and CHONS compounds, while CHO compounds are less represented. When exposed to light under dry conditions, there is a noticeable decrease in peak intensity and a shift of CHOS signals towards higher oxidation states in the Van Krevelen diagram suggesting possible oxidation and photolysis of the native organic matter. The fact that the ACSM showed an invariant oxidation state suggests that the changes may involve a minor fraction of the native organic matter with higher ionisation potential in ESI Orbitrap. Under humid conditions, no appreciable changes in oxidation state or peak number have been observed by ESI

The bulk composition analysed by ESI Orbitrap probably consists predominantly of lipidic and proteinaceous compounds, as indicated by the presence of signals from molecules containing C, H, O, N, and S. In particular, the O/C ratio measured with the highest frequency remains in fact relatively stable across the four conditions (dark and irradiated, in both dry and 80% relative humidity environments). In the dry condition, the dark samples show a peak O/C ratio around 0.2, indicating that the most common compounds have a relatively low level of oxidation. When these samples are irradiated, the O/C ratio with the highest frequency shifts slightly higher, peaking around 0.3 to 0.4. At 80% RH condition, the dark samples maintain a similar O/C ratio peak near 0.2, comparable to the dry dark samples. Under irradiation at 80% RH, the O/C ratio at maximum frequency remains stable, with values between 0.1 and 0.2, showing consistency across the different conditions.

Finally, and most importantly, the analysis does not detect any glyoxal-related organic compounds, which is the necessary baseline for interpreting the results of the uptake experiments.

To the best of our knowledge, to date there is only one publication presenting the characterization of the native particulate dust organic fraction on a laboratory scale. In this study (Marsden et al. 2018), the observation of CN^- and CNO^+ signals in mass spectra from individual dust particles originating from Sahel and Morocco revealed an internally mixed biological content before emission. The presence of CN and CNO signals in dust mass spectra is a significant indicator of nitrogen-containing organic compounds, which are often of biological origin. This mixing of biological material with dust is of particular interest because it can affect not only the chemical composition of dust but also its environmental and health implications. For instance, the transport of dust particles containing microorganisms has been linked to human health concerns, as highlighted by studies on the transport of bacteria through dust storms (Yamaguchi et al., 2012).

S4.3. SFE-GC-MS

Figure S4.3 shows the chromatograms from the SFE-GC-MS analysis of Gobi dust's organic fraction.

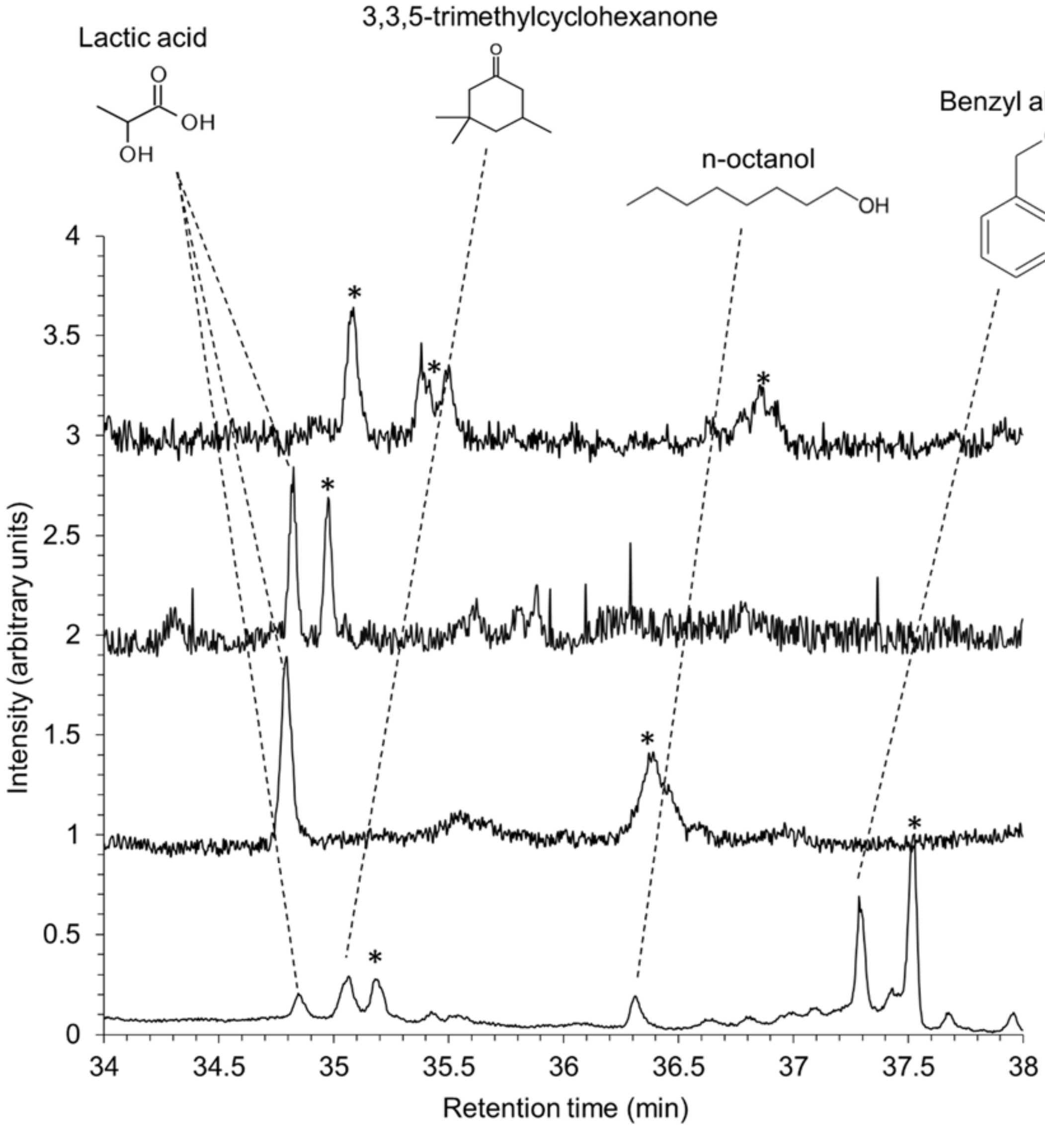

Figure S4.3. Chromatograms from SFE-GC-MS analysis of Gobi dust under four different conditions, from top to bottom: (1) dry, dark; (2) dry, light; (3) RH 80%, dark; (4) RH 80%, light. The retention time interval between 34 and 38 minutes was selected for analysis due to the absence of significant peaks before 34 minutes and the presence of internal standards after 38 minutes. The peaks marked with asterisks are those that remained unassigned.

In Figure S4.3, the chromatograms display a retention time interval between 34 and 38 minutes. This specific interval is chosen because no significant peaks are detected before 34 minutes, while after 38 minutes, the chromatograms are dominated by the signals from the two added internal standards. Beside, they become too noisy, making it difficult to extract reliable chemical information.

In the temporal window under analysis, the chromatograms exhibit poor reproducibility across different experimental conditions.

Some compounds are identified. Lactic acid is found in three out of the four chromatograms, but not in dry and dark conditions. Other compounds, such as 3,3,5-trimethylcyclohexanone, n-octanol, and benzyl alcohol, were only detected in the sample processed under irradiation at 80% RH. We exclude the possibility that these compounds originate from a photochemical transformation of the organic material in the dust, as the corresponding chromatogram of the sample collected in dark conditions does not show the precursor products that we observe under irradiation. This suggests that compounds are part of the dust's organic content but are not consistently detected across all conditions. Several peaks marked with asterisks remain unassigned, as the corresponding mass spectra did not match reference spectra in the NIST library with sufficient probability (≥80%).

Despite the observed variability, the key finding is that none of the detected compounds are related to glyoxal. In summary, the results indicate that the organic composition of dust aerosols is shaped less by experimental conditions (humidity, light) and more by the inherent variability of the dust itself. Crucially, no glyoxal-related compounds were detected, reinforcing the reliability of glyoxal-related findings in subsequent analyses.

The compounds detected in our GC-MS analysis, such as levulinic acid and lactic acid, could share a biological origin with the CN and CNO signals already observed in dust particle mass spectra. Both results suggest that biological material or its degradation products are mixed with the dust aerosol, contributing to the complexity of the organic fraction (Carr et al., 2002; Kim et al., 2024). In prior investigations concerning organic acids in dust samples, a variety of linear (C1-C10), branched chain, and hydroxy (lactic and glycolic) monoacids in dust samples was observed. Notably, lactic acid was abundant in aerosol samples collected from North East China, attributed to microbial and plant sources (Mochizuki et al., 2018). Kawamura et al. (2000) analysed urban dust and soil samples from the atmosphere of Los Angeles and detected carboxylic acids in the dust organic fraction. Organic acids were not detected in the soils, but only in the dust samples at concentrations ranging from 200-770 nmol g-1. Benzoic acid was detected in dust samples, while we detect its reduced form (benzylic alcohol).

Furthermore, GC analysis from Gobi dust samples (< 10 μm) from Mt. Tateyama (Japan) indicates the presence of lactic and glycolic acids (Mochizuki et al., 2016). The authors suggest that these organic acids are adsorbed onto dust particles during transport, making dust particles carriers of volatile and semi-volatile organic acids.

References of the Supplementary Material

Alves, C., Oliveira, T., Pio, C., Silvestre, A. J. D., Fialho, P., Barata, F., and Legrand, M.: Characterisation of carbonaceous aerosols from the Azorean Island of Terceira, Atmos. Environ., 41, 1359–1373, https://doi.org/10.1016/j.atmosenv.2006.10.022, 2007.

Aymoz, G., Jaffrezo, J. L., Jacob, V., Colomb, A., and George, C.: Evolution of organic and inorganic components of aerosol during a Saharan dust episode observed in the French Alps, Atmos. Chem. Phys., 4, 2499-2512, 10.5194/acp-4-2499-2004, 2004.

Carr, F. J., Chill, D., and Maida, N.: The Lactic Acid Bacteria: A Literature Survey, Critical Rev. Microbiology, 28, 281–370, https://doi.org/10.1080/1040-840291046759, 2002.

Conen, F., Morris, C. E., Leifeld, J., Yakutin, M. V., and Alewell, C.: Biological residues define the ice nucleation properties of soil dust, Atmos. Chem. Phys., 11, 9643–9648, https://doi.org/10.5194/acp-11-9643-2011, 2011.

Denjean, C., Formenti, P., Picquet-Varrault, B., Pangui, E., Zapf, P., Katrib, Y., Giorio, C., Tapparo, A., Monod, A., Temime-Roussel, B., Decorse, P., Mangeney, C., and Doussin, J. F.: Relating hygroscopicity and optical properties to chemical composition and structure of secondary organic aerosol particles generated from the ozonolysis of α-pinene, Atmos. Chem. Phys., 15, 3339–3358, https://doi.org/10.5194/acp-15-3339-2015, 2015.

Galloway, M. M., Chhabra, P. S., Chan, A. W. H., Surratt, J. D., Flagan, R. C., Seinfeld, J. H., and Keutsch, F. N.: Glyoxal uptake on ammonium sulphate seed aerosol: reaction products and reversibility of uptake under dark and irradiated conditions, Atmos. Chem. Phys., 9, 3331–3345, https://doi.org/10.5194/acp-9-3331-2009, 2009.

Gonçalves, C., Alves, C., Nunes, T., Rocha, S., Cardoso, J., Cerqueira, M., Pio, C., Almeida, S. M., Hillamo, R., and Teinilä, K.: Organic characterisation of PM10 in Cape Verde under Saharan dust influxes, Atmos. Environ., 89, 425–432, https://doi.org/10.1016/j.atmosenv.2014.02.025, 2014.

Griffin, D. W.: Atmospheric Movement of Microorganisms in Clouds of Desert Dust and Implications for Human Health, Clin Microbiol Rev, 20, 459–477, https://doi.org/10.1128/CMR.00039-06, 2007.

Kawamura, K., Steinberg, S., and Kaplan, I. R.: Homologous series of C1–C10 monocarboxylic acids and C1–C6 carbonyls in Los Angeles air and motor vehicle exhausts, Atmos. Environ., 34, 4175–4191, https://doi.org/10.1016/S1352-2310(00)00212-0, 2000.

Kim, H. J., Kim, B. C., Park, H., Cho, G., Lee, T., Kim, H. T., Bhatia, S. K., and Yang, Y.-H.: Microbial production of levulinic acid from glucose by engineered Pseudomonas putida KT2440, J. Biotechnology, S016816562400258X, https://doi.org/10.1016/j.jbiotec.2024.09.015, 2024.

Lai, A. C., Nazaroff, W. W. Modeling indoor particle deposition from turbulent flow onto smooth surfaces. J. Aerosol Sci., 31(4), 463-476, 2000.

Jung, C. and Schindler, D.: The role of air density in wind energy assessment – A case study from Germany, Energy, 171, 385–392, https://doi.org/10.1016/j.energy.2019.01.041, 2019.

Kostenidou, E., Pathak, R. K., and Pandis, S. N.: An Algorithm for the Calculation of Secondary Organic Aerosol Density Combining AMS and SMPS Data, Aerosol Science and Technology, 41, 1002–1010, https://doi.org/10.1080/02786820701666270, 2007.

Lamkaddam, H.. Etude en atmosphère simulée de la formation d'Aérosol Organique Secondaire issue de la photooxydation du n-dodécane: impact des paramètres environnementaux. Diss. Université Paris-Est, 2017.

Lepple, F. K. and Brine, C. J.: Organic constituents in eolian dust and surface sediments srom northwest Africa, J. Geophys. Res., 81, 1141–1147, https://doi.org/10.1029/JC081i006p01141, 1976.

Marsden, N. A., Ullrich, R., Möhler, O., Eriksen Hammer, S., Kandler, K., Cui, Z., Williams, P. I., Flynn, M. J., Liu, D., Allan, J. D., and Coe, H.: Mineralogy and mixing state of north African mineral dust by online single-particle mass spectrometry, Atmos. Chem. Phys., 19, 2259–2281, https://doi.org/10.5194/acp-19-2259-2019, 2019.

Mochizuki, T., Kawamura, K., Aoki, K., and Sugimoto, N.: Long-range atmospheric transport of volatile monocarboxylic acids with Asian dust over a high mountain snow site, central Japan, Atmos. Chem. Phys., 16, 14621–14633, https://doi.org/10.5194/acp-16-14621-2016, 2016.

Mochizuki, T., Kawamura, K., Miyazaki, Y., and Boreddy, S. K. R.: Distributions and sources of gaseous and particulate low molecular weight monocarboxylic acids in a deciduous broadleaf forest from northern Japan, Aerosols/Field Measurements/Troposphere/Chemistry (chemical composition and reactions), https://doi.org/10.5194/acp-2018-444, 2018.

O'Sullivan, D., Murray, B. J., Malkin, T. L., Whale, T. F., Umo, N. S., Atkinson, J. D., Price, H. C., Baustian, K. J., Browse, J., and Webb, M. E.: Ice nucleation by fertile soil dusts: relative importance of mineral and biogenic components, Atmos. Chem. Phys., 14, 1853–1867, https://doi.org/10.5194/acp-14-1853-2014, 2014.

Simoneit, B. R. T.: Eolian particulates from oceanic and rural areas—their lipids fulvic and humic acids and residual carbon, Physics and Chemistry of the Earth, 12, 343–352, https://doi.org/10.1016/0079-1946(79)90117-4, 1980.

Srivastava, D., Tomaz, S., Favez, O., Lanzafame, G. M., Golly, B., Besombes, J.-L., Alleman, L. Y., Jaffrezo, J.-L., Jacob, V., Perraudin, E., Villenave, E., and Albinet, A.: Speciation of organic fraction does matter for source apportionment. Part 1: A one-year campaign in Grenoble (France), Sci. Tot. Environ., 624, 1598–1611, https://doi.org/10.1016/j.scitotenv.2017.12.135, 2018.

Von der Weiden, S-L., F. Drewnick, and S. J. A. M. T. Borrmann. "Particle Loss Calculator–a new software tool for the assessment of the performance of aerosol inlet systems. Atmos. Meas. Tech. 2.2: 479-494, 2009.

Webb, Nicholas P., Sandra L. LeGrand, Brad F. Cooper, Ericha M. Courtright, Brandon L. Edwards, Christopher Felt, Justin W. Van Zee, and Nancy P. Ziegler. "Size distribution of mineral dust emissions from sparsely vegetated and supply-limited dryland soils." J. Geophys. Res., 126, 22, https://doi.org/10.1029/2021JD035478, 2021.